Eurographics / IEEE Symposium on Visualization 2011 (EuroVis 2011)
H. Hauser, H. Pfister, and J. J. van Wijk
(Guest Editors)

Volume 30 (2011), Number 3

Topological Features in 2D Symmetric Higher-Order Tensor Fields

T. Schultz

Computation Institute, University of Chicago, USA — t.schultz@uchicago.edu

Abstract

The topological structure of scalar, vector, and second-order tensor fields provides an important mathematical basis for data analysis and visualization. In this paper, we extend this framework towards higher-order tensors. First, we establish formal uniqueness properties for a geometrically constrained tensor decomposition. This allows us to define and visualize topological structures in symmetric tensor fields of orders three and four. We clarify that in 2D, degeneracies occur at isolated points, regardless of tensor order. However, for orders higher than two, they are no longer equivalent to isotropic tensors, and their fractional Poincaré index prevents us from deriving continuous vector fields from the tensor decomposition. Instead, sorting the terms by magnitude leads to a new type of feature, lines along which the resulting vector fields are discontinuous. We propose algorithms to extract these features and present results on higher-order derivatives and higher-order structure tensors.

Categories and Subject Descriptors (according to ACM CCS): I.4.7 [Image Processing and Computer Vision]: Feature Measurement—Invariants

1. Introduction

Feature extraction is a common strategy to deal with the large and complex datasets generated by modern scientific experiments and simulations. In visualization, topological methods are an established way of finding geometric features such as structurally important points, curves, or surfaces in spatial data. As a preprocess for interactive visualization, this reduces the amount of information the rendering pipeline and the user need to handle. For the scientist, the features might be the objects of ultimate interest, or they may guide subsequent analysis with other tools.

Topological methods are most widely used to visualize scalar [BPS98] and vector fields [HH89, PVH*03]. Topological features have also been extracted from second-order tensor fields, both symmetric [DH94,TSH01,ZPP05,STS07, SNAHH11] and asymmetric [ZP05,ZYLL09]. However, we are not aware of any attempts to define topological features in higher-order tensor fields, which arise in applications like diffusion MRI [ÖM03, HS05, SS08], computer vision [SWS09], or when considering the higher-order derivatives of any smooth scalar field.

This gap in the visualization literature is unfortunate, since problems such as high information density, which have contributed to the popularity of topological methods in vector and second-order tensor data, are even more grave in higher-order tensor fields. We believe that the lack of suitable tools for visualization contributes to the fact that higher-order derivatives are used only rarely and higher-order tensors are picked up only reluctantly as a more general mathematical model. Therefore, it is the goal of this paper to explore topological features in higher-order tensor fields.

For this initial study, we consider steady symmetric 2D tensor fields of orders three and four. We formally characterize the uniqueness properties of a constrained higher-order tensor decomposition and use it to define vector fields that hold all the information from the tensors. Topological features in those fields include degenerate points and lines along which the fields are discontinuous, a novel type of feature that is not present in second-order tensor topology. Experiments substantiate the applicability of the resulting algorithms for feature extraction.

2. Background and Related Work

2.1. General Notions

We define a field to be a C^k continuous function $f : D \to R$ on a compact domain $D \subset \mathbb{R}^d$. The exact order of differen-

tiability k will be assumed as needed. The codomain R of a scalar field is $\mathbb{R}$; for a vector field, it is $\mathbb{R}^r$; for a symmetric second-order tensor field, it is $\mathbb{R}^{r\times r}$; higher-order tensor fields are defined accordingly (e.g., $\mathbb{R}^{r\times r\times r}$ in the third-order case). In all our examples, the dimensions in the domain and codomain agree, $r = d = 2$.

Topological analysis often focuses on generic properties. Formally, a property is generic in some topological space X iff there exists an open dense subset $U \subset X$ that has the desired property. In practice, this guarantees that the property is preserved under small perturbations, and that any element of X that does not have the property can be approximated arbitrarily closely by another element that does.

2.2. Vector Field Topology

The topological analysis of a steady vector field $\mathbf{f}(\mathbf{x})$ is based on its streamlines, the trajectories of massless particles that are advected by $\mathbf{f}$. Streamlines stop when $\|\mathbf{f}(\mathbf{x})\| = 0$. When the dimensions of the domain and the codomain of a vector field agree and in the absence of constraints (such as no-slip boundaries), this generically happens at isolated critical points. Based on the vector field Jacobian, they are classified as saddles, attracting or repelling nodes or foci, or centers [HH89]. In 2D, additional points of interest occur near walls (attachment and detachment nodes) and at the boundary of the domain (incoming and outgoing points).

The topological skeleton of a 2D vector field consists of these isolated points, the streamlines that connect to saddles (separatrices), and periodic orbits. It partitions the domain of the field into regions of uniform asymptotic behavior, i.e., all streamlines in the same region start and end in a common critical point, closed streamline, or segment of a boundary.

2.3. Second-Order Tensor Field Topology

An $n \times n$ symmetric matrix $\mathbf{T}$ can be written in terms of n real eigenvalues λ_i and orthonormal eigenvectors $\mathbf{v}_i$:

$$\mathbf{T} = \sum_{i=1}^{n} \lambda_i \mathbf{v}_i \otimes \mathbf{v}_i. \tag{1}$$

Based on this spectral decomposition of a tensor field $\mathbf{T}(\mathbf{x})$, we may define n eigenvector fields $\bar{\mathbf{v}}_i(\mathbf{x}) = \lambda_i(\mathbf{x})\mathbf{v}_i(\mathbf{x})$ that contain all the information of the original tensor field. The orientation in eigenvector fields is undefined, $\bar{\mathbf{v}}_i$ and $-\bar{\mathbf{v}}_i$ are equivalent, but tangent curves (hyperstreamline trajectories [DH93]) can still be integrated.

In the framework of Delmarcelle and Hesselink [DH94], tensor field topology is defined to be the topology of the derived eigenvector fields. The locations $\mathbf{x}$ at which hyperstreamlines in $\bar{\mathbf{v}}_i(\mathbf{x})$ stop are places in which $\lambda_i(\mathbf{x}) = \lambda_j(\mathbf{x})$ for at least one $j \neq i$. In this case, the spectral decomposition is not unique, since $\mathbf{v}_i$ and $\mathbf{v}_j$ can be replaced by any orthonormal pair $\tilde{\mathbf{v}}_i$ and $\tilde{\mathbf{v}}_j$ that spans the same space. In unconstrained 2D data, this generically happens at isolated points, which are called degenerate points and take the place of critical points in vector field topology. Zheng et al. [ZPP05] have transferred this framework to 3D, where degeneracies form structurally stable features lines. Our work presents a different generalization, to 2D higher-order tensor fields.

2.4. Higher-Order Tensors

The coefficients $t_{i_1 i_2 \ldots i_\ell}$ of an order-ℓ tensor $\mathcal{T}$ with respect to some basis form a multi-way array with ℓ indices, each ranging from 1 to the dimension of the tensor. The coefficients of a symmetric tensor are invariant under any index permutation σ: $t_{i_1 i_2 \ldots i_\ell} = t_{i_{\sigma(1)} i_{\sigma(2)} \ldots i_{\sigma(\ell)}}$. This greatly reduces the number of free parameters in the tensor, from 2^ℓ to $\ell + 1$ for a two-dimensional tensor. When writing out tensor coefficients, we will only consider these non-redundant entries.

In recent years, applications and decompositions of higher-order tensors have been an active topic of research. An excellent introduction is given by Kolda and Bader [KB09]. Within the visualization community, there is still relatively little work on higher-order tensors. Hlawitschka and Scheuermann [HS05] define a higher-order analog of hyperstreamlines; Schultz and Seidel [SS08] use low-rank tensor approximation to achieve more accurate fiber estimates in diffusion MRI. From fourth-order tensors that occur in solid mechanics, Neeman et al. [NBJ*08] extract second-order tensors that can be visualized with traditional tensor glyphs. Schultz and Kindlmann [SK10] present a sharpened glyph for symmetric higher-order tensors. None of these previous works have followed a feature-based visualization approach, which is the main focus of our paper.

Palacios and Zhang [PZ07] have used symmetric 2D order-ℓ tensor fields to represent ℓ-way rotational symmetries, which play a role in remeshing and pen-and-ink surface sketching. Even though the authors provide a topological analysis of singularities and separatrices, their analysis is specific to rotational symmetries, which form a two-dimensional linear subspace of the $\ell+1$-dimensional higher-order tensor space. Therefore, these existing results do not carry over to the more general case discussed in our paper.

3. Higher-Order Tensor Field Topology

We will generalize vector field topology to higher order tensors by deriving a set of vector fields that contain all the information from the tensors, and considering their topology.

3.1. The Canonical Decomposition

A symmetric rank-1 matrix is defined as the outer product $\mathbf{v} \otimes \mathbf{v}$ of some vector $\mathbf{v}$ with itself. In analogy, a symmetric rank-1 order-ℓ tensor is defined as the ℓ-fold outer product, which we denote by $\mathbf{v}^{\otimes\ell}$. Any symmetric tensor $\mathcal{T}$ can be

written as a sum of symmetric rank-1 terms,

$$\mathcal{T} = \sum_{i=1}^{R} \lambda_i \mathbf{v}_i^{\otimes \ell}, \tag{2}$$

where we assume that all $\mathbf{v}_i$ are normalized and scaling is performed through the λ_i [CGLM08]. The symmetric tensor rank is defined as the smallest integer R for which an exact decomposition is possible. Eq. (2) is known as the symmetric outer product decomposition, or the symmetric canonical decomposition. In an alternative, but equivalent formulation, it has been studied in considerable depth by Reznick [Rez92].

3.2. A Geometrically Constrained Decomposition

Even though Eq. (2) can be regarded as a generalization of the spectral decomposition, it does not define vector fields suitable for topological analysis, since the result may not be unique. In fact, there is a one-dimensional fiber of solutions for all even-order 2D tensors [CM96]. This is also true for second-order tensors; the only reason why the spectral decomposition in Eq. (1) is generically unique is the orthogonality constraint on the $\mathbf{v}_i$.

Kyrgyzov and Erdogmus [KE10] argue that a natural relaxation of orthogonality for n two-dimensional vectors is a fixed spacing of π/n between neighbors. Consequently, they propose to decompose symmetric order-ℓ tensors with a fixed frame of ℓ rank-1 terms:

$$\mathcal{T} = \sum_{i=1}^{\ell} \lambda_i \mathbf{v}_i^{\otimes \ell} \quad \text{with } \mathbf{v}_i = \begin{pmatrix} \cos(-\theta + (i-1)\pi/\ell) \\ \sin(-\theta + (i-1)\pi/\ell) \end{pmatrix}. \tag{3}$$

This geometrically constrained decomposition has $\ell + 1$ degrees of freedom: ℓ in the λ_i, and one more in the angle θ, which determines the joint rotation of the $\mathbf{v}_i$. Since this matches the number of free parameters in the symmetric tensor $\mathcal{T}$, Kyrgyzov [Kyr10] expresses the hope that Eq. (3) might offer a one-to-one reparameterization. However, an equal number of parameters is not a sufficient condition for uniqueness, and no formal proof has been presented.

Two key contributions of our work are a proof that, at least for orders $\ell = 3$ and $\ell = 4$, this constrained decomposition always exists, and a full characterization of the cases in which it is unique. Our analysis reveals that some tensors $\mathcal{T}$ can be written in the form of Eq. (3) regardless of the choice of θ. Since these tensors do not possess a unique constrained decomposition, we treat them as a higher-order analog of degenerate tensors in second-order fields, which provide the geometric features of central interest in topological visualization: Degenerate points in 2D [DH94] and degenerate lines in 3D [ZPP05].

3.3. Analytical Solution

In order to find the rotation θ in their constrained decomposition, Kyrgyzov and Erdogmus [KE10] explore various optimization techniques. The definition of topological features in higher-order tensor fields requires an analytical solution.

Our strategy for its derivation is analogous to the Jacobi method for matrix diagonalization, which is explained briefly in Section 3.3.1. We observe that when the angle θ in Eq. (3) is known, the higher-order tensor can be written in a special form. In analogy to the diagonal form of a second-order tensor, it allows us to easily solve for the λ_i. We then derive an analytical solution for the value of θ. Except for the degenerate cases that will be used to define topological features, there are ℓ isolated solutions within $\theta \in (-\pi, \pi]$, corresponding to reorderings of the terms in Eq. (3). Our analysis is for tensors of orders three and four, but we conjecture that it carries over to 2D tensors of arbitrary order.

3.3.1. The Second-Order Case

When a symmetric second-order tensor $\mathbf{T}$ is written in a basis that consists of its orthonormal eigenvectors ($\mathbf{v}_1 = (1,0)^{\mathrm{T}}$, $\mathbf{v}_2 = (0,1)^{\mathrm{T}}$), its coefficient matrix becomes diagonal, with the eigenvalues λ_i as diagonal elements:

$$\mathbf{T} = \begin{pmatrix} \lambda_1 & 0 \\ 0 & \lambda_2 \end{pmatrix}. \tag{4}$$

Given a general symmetric matrix with entries t_{ij}, the angle θ by which the matrix needs to be rotated to attain diagonal form can be found by solving

$$\tan(2\theta)(t_{22} - t_{11}) = 2t_{12} \tag{5}$$

for θ [Jac46]. When $\mathbf{T}$ is isotropic ($\mathbf{T} = \alpha\mathbf{I}$, where $\mathbf{I}$ is the identity matrix), both sides of Eq. (5) are zero, regardless of θ. This is the degenerate case on which topological visualization of 2D second-order tensor fields is founded.

3.3.2. The Third-Order Case

Let us now consider the coefficients of a symmetric third-order tensor when the first basis vector is aligned with the vector $\mathbf{v}_1$ in the decomposition, i.e.,

$$\mathbf{v}_1 = \begin{pmatrix} 1 \\ 0 \end{pmatrix} \quad \mathbf{v}_2 = \begin{pmatrix} 1/2 \\ \sqrt{3/4} \end{pmatrix} \quad \mathbf{v}_3 = \begin{pmatrix} -1/2 \\ \sqrt{3/4} \end{pmatrix}. \tag{6}$$

Substituting into Eq. (3) gives the tensor coefficients

$$\begin{aligned} t_{111} &= \lambda_1 + \frac{1}{8}(\lambda_2 - \lambda_3) & t_{112} &= \sqrt{\frac{3}{64}}(\lambda_2 + \lambda_3) \\ t_{122} &= \frac{3}{8}(\lambda_2 - \lambda_3) & t_{222} &= \sqrt{\frac{27}{64}}(\lambda_2 + \lambda_3). \end{aligned} \tag{7}$$

Eq. (7) reveals that when the tensor is in this canonical frame, t_{112} and t_{222} are linearly dependent,

$$t_{222} - 3t_{112} = 0. \tag{8}$$

This condition is analogous to the diagonality constraint in the second-order case ($t_{12} = 0$) in the sense that it allows

for simple computation of the scalars λ_i in Eq. (3), by solving the linear system in Eq. (7):

$$\lambda_1 = t_{111} - \frac{1}{3}t_{122} \quad \lambda_2 = \frac{4}{\sqrt{3}}t_{112} + \frac{4}{3}t_{122} \\ \lambda_3 = \frac{4}{\sqrt{3}}t_{112} - \frac{4}{3}t_{122}. \tag{9}$$

In analogy to the Jacobi rotation in Eq. (5), we can compute the angle θ by which we need to rotate the third-order tensor such that Eq. (8) holds. It is found by writing the coefficients $\tilde{t}_{112}$ and $\tilde{t}_{222}$ of a rotated tensor $\tilde{\mathcal{T}}$ in terms of the rotation angle θ and the original coefficients of $\mathcal{T}$. Let $c = \cos(\theta)$ and $s = \sin(\theta)$. Then,

$$\begin{aligned} \tilde{t}_{112} &= c^2 s t_{111} + (c^3 - 2cs^2)t_{112} + \\ &\quad (s^3 - 2c^2 s)t_{122} + s^2 c t_{222} \\ \tilde{t}_{222} &= s^3 t_{111} + 3s^2 c t_{112} + 3sc^2 t_{122} + c^3 t_{222}. \end{aligned} \tag{10}$$

After substituting this into Eq. (8), algebraic simplification and trigonometric equalities yield

$$\tan(3\theta)\,(t_{111} - 3t_{122}) = t_{222} - 3t_{112}. \tag{11}$$

Within $\theta \in (-\pi, \pi]$, this equation has three solutions. They correspond to reorderings of λ_i and the corresponding $\mathbf{v}_i$, so generically, the decomposition in Eq. (3) is indeed unique up to these trivial permutations. After the rotation, the λ_i are given by Eq. (9). The degeneracy that we will use for topological visualization of third-order tensor fields occurs when Eq. (11) holds for all θ. This happens iff

$$t_{111} - 3t_{122} = 0 \quad \text{and} \quad t_{222} - 3t_{112} = 0. \tag{12}$$

3.3.3. The Fourth-Order Case

The symmetric fourth-order case can be treated in full analogy to the previous section. When writing the tensor coefficients t_{ijkl} in the basis whose first vector is aligned with $\mathbf{v}_1$, we find the linear dependence

$$t_{1112} = t_{1222}, \tag{13}$$

leading to the following formulas for λ_i:

$$\lambda_1 = t_{1111} - t_{1122} \quad \lambda_2 = 2(t_{1122} + t_{1112}) \\ \lambda_3 = t_{2222} - t_{1122} \quad \lambda_4 = 2(t_{1122} - t_{1112}). \tag{14}$$

A Jacobi-like angle θ can be computed from

$$\tan(4\theta)(t_{1111} + t_{2222} - 6t_{1122}) = 4(t_{1222} - t_{1112}). \tag{15}$$

The four solutions within $\theta \in (-\pi, \pi]$ again correspond to reorderings of the terms in Eq. (3), and a degenerate case, in which θ is undetermined, occurs when

$$t_{1111} + t_{2222} - 6t_{1122} = 0 \quad \text{and} \quad t_{1222} - t_{1112} = 0. \tag{16}$$

3.4. Isotropic vs. Degenerate Tensors

Isotropic matrices, $\mathbf{T} = \alpha\mathbf{I}$, exhibit rotational invariance: Their quadratic form $T(\mathbf{x}) = \mathbf{x}^{\mathrm{T}}\mathbf{T}\mathbf{x}$ is constant for all unit-length $\mathbf{x}$. Similarly, we call a higher-order tensor $\mathcal{T}$ isotropic iff its homogeneous form $T(\mathbf{x}) = \mathcal{T} \cdot^{\ell} \mathbf{x}$ (the ℓ-fold inner product between $\mathcal{T}$ and $\mathbf{x}$) is constant on the unit circle.

Since the homogeneous forms of odd-order tensors are odd functions, $T(-\mathbf{x}) = -T(\mathbf{x})$, the only isotropic odd-order tensors are zero tensors. Even-order isotropic tensors are obtained by setting all λ_i in Eq. (3) to some common value. It is known [SWS09] that the average of $T(\mathbf{x})$ over the unit circle for an even-order rank-1 tensor $\mathcal{T} = \lambda\mathbf{v}^{\otimes\ell}$ equals

$$\frac{1}{2\pi}\int_{\|\mathbf{x}\|=1} T(\mathbf{x})\,d\mathbf{x} = \lambda\frac{(\ell-1)!!}{\ell!!}, \tag{17}$$

where the double factorial $\ell!!$ is defined via the recursion $\ell!! = \ell \times (\ell-2)!!$, $1!! = 0!! = 1$. It follows that we obtain an even-order tensor $\mathcal{I}^{(\ell)}$ whose homogeneous form is unity on the unit circle if we choose $\lambda_i = (\ell-2)!!/(\ell-1)!!$. All other isotropic tensors are multiples of it,

$$\mathcal{T} = \alpha\mathcal{I}^{(\ell)}. \tag{18}$$

In Section 3.2, we have defined degenerate tensors as tensors $\mathcal{T}$ that can be written in the form of Eq. (3) for all choices of θ. For matrices ($\ell = 2$), the isotropic and the degenerate case coincide. For $\ell = 3$ and $\ell = 4$, the definition of degeneracy leads to two independent linear constraints, i.e., it is fulfilled within a subspace of codimension two. Isotropic tensors form a zero-dimensional (odd ℓ) or a one-dimensional (even ℓ) proper subspace of these degenerate tensors. Thus, a subspace of tensors with order $\ell > 2$ are degenerate, but not isotropic. For these tensors, Eq. (3) has an indeterminacy that does not simply amount to reordering the terms, and which is not caused by a lack of orientational information in the tensor (i.e., isotropy).

Fig. 1 illustrates a third-order (a) and a fourth-order (b) example of such a non-isotropic degeneracy. The respective tensor is shown with a polar plot $\mathbf{p}(\mathbf{x}) = |T(\mathbf{x})|\,\mathbf{x}$ for $\|\mathbf{x}\| = 1$, where color indicates the sign of $T(\mathbf{x})$ (red is positive, blue is negative). We also show the scaled vectors $\bar{\mathbf{v}}_i = \lambda_i\mathbf{v}_i$, which contain all information from the tensor. For even ℓ, the vectors are without orientation, i.e., $\bar{\mathbf{v}}_i$ and $-\bar{\mathbf{v}}_i$ are equivalent, so we show them as line segments (since all λ_i in our example are positive, we do not use color coding here).

From different choices of θ, we get different decompositions that all fulfill the constraint in Eq. (3), and all sum to the same tensor, $t_{111} = 0$, $t_{112} = 1$, $t_{122} = 0$, $t_{222} = 3$ in (a) and $t_{1111} = 2$, $t_{1112} = 0$, $t_{1122} = 1$, $t_{1222} = 0$, $t_{2222} = 4$ in (b). The two-dimensional subspace of degenerate third-order tensors is spanned by scaling and rotating the example in (a). In addition to rotation and scaling, the three-dimensional subspace of degenerate fourth-order tensors accounts for adding any multiple $\alpha\mathcal{I}^{(4)}$ of the identity.

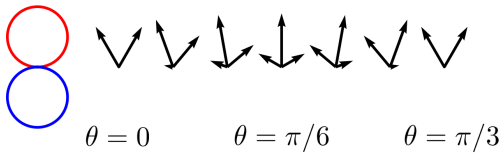

(a) Possible decompositions of a degenerate third-order tensor.

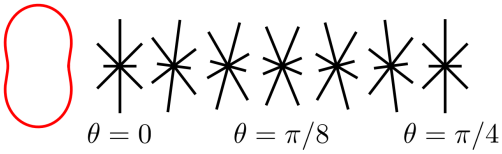

(b) Possible decompositions of a degenerate fourth-order tensor.

Figure 1: *Even though these higher-order tensors are not isotropic, they do not have a unique decomposition into geometrically constrained rank-1 terms. All other degenerate cases can be derived from the examples visualized here.*

3.5. Topological Features in Derived Vector Fields

3.5.1. Degenerate Points

We have seen above that, at least for $\ell \in \{2,3,4\}$, degeneracies form a subspace A of codimension two within the space of all 2D order-ℓ tensors. Due to its two spatial dimensions, the tensor field forms a 2D subspace B in the same $\ell+1$-dimensional space, i.e., a space of codimension $\ell-1$. Assuming non-degenerate configurations of the fields, the occurance of a degeneracy within the 2D field lies in the transversal intersection of A and B, so $\mathrm{codim}(A \cap B) = \mathrm{codim}(A) + \mathrm{codim}(B) = 2+\ell-1 = \ell+1$. Since this equals the dimensionality of the full order-ℓ tensor space, we will generically observe zero-dimensional degeneracies, degenerate points, regardless of the tensor order ℓ. This reasoning is analogous to the proofs given by Damon [Dam98] and by Zheng et al. [ZPP05] for the fact that degeneracies in second-order 3D tensor fields form lines; we refer to these papers for a more formal treatment of transversal intersections.

Even-order isotropic tensors form a subspace of codimension ℓ. By the same argument, their dimensionality in order-ℓ 2D tensor fields is $2-\ell$. This means that generically, they only occur in second-order fields, where they coincide with degenerate points. If they occur in the higher-order case, they can be transformed into a non-isotropic degeneracy by an arbitrarily small perturbation.

3.5.2. Poincaré Index of Degenerate Points

An important property of a critical point in a vector field $\mathbf{v}(\mathbf{x})$ is its Poincaré index, defined as the number of counterclockwise revolutions of the vector $\mathbf{v}(\mathbf{x})$, as $\mathbf{x}$ moves in counterclockwise direction along a closed curve that contains the critical point in question, but no other degeneracy.

We adapt this definition of the Poincaré index by considering rotations of the frame of all $\mathbf{v}_i$ in Eq. (3) as a whole. The angle θ of the frame is given in Eq. (11) and Eq. (15) as

$$q\tan(\ell\theta) = p, \tag{19}$$

where p and q are linear functions of tensor coefficients and, by definition, $p = q = 0$ at the degeneracy.

In analogy to vector [HH89] and second-order tensor topology [DH94], we investigate degeneracies based on a first-order approximation of the tensor field. If we parameterize a circle around the degeneracy by $\psi \in [0, 2\pi)$, the first-order approximation of p and q can be written as

$$p(\psi) \approx \hat{p}\sin(\psi + \psi_0^{(p)}) \quad q(\psi) \approx \hat{q}\sin(\psi + \psi_0^{(q)}). \tag{20}$$

Substituting Eq. (20) into Eq. (19) reveals that along the circle, $\ell\theta$ takes on each value in $(-\pi, \pi]$ exactly once, rotating the frame of all $\mathbf{v}_i$ in Eq. (3) by $\pm 2\pi/\ell$. For $\ell = 2$, this leads to the well-known Poincaré indices of trisectors $(-1/2)$ and wedges $(1/2)$ [DH94]. The fact that they are half-integers reflects the non-orientability of eigenvectors in the presence of a degeneracy. For $\ell > 2$, a Poincaré index of $\pm 1/\ell$ makes it impossible to partition the ℓ vectors from the decomposition into ℓ vector fields without introducing discontinuities that originate in degeneracies.

Fig. 2 illustrates this with examples from a third- (a) and a fourth-order field (b): Along a closed curve around the degeneracy, the joint frames of three and four vectors, respectively, vary continuously. However, when we follow any individual vector (e.g., the one marked in cyan), we find that when we return to the initial starting point, the vector has not been rotated back to the vector that we started with, but to a different vector in the same frame, $\pm 2\pi/\ell$ apart.

The Poincaré index of a degeneracy in a second-order tensor field is known to be $\frac{1}{2}\mathrm{sign}(ad-bc)$ [DH94], where:

$$\begin{aligned} a &= \frac{1}{2}\frac{\partial(t_{11}-t_{22})}{\partial x} & b &= \frac{1}{2}\frac{\partial(t_{11}-t_{22})}{\partial y} \\ c &= \frac{\partial t_{12}}{\partial x} & d &= \frac{\partial t_{12}}{\partial y}. \end{aligned} \tag{21}$$

From Eq. (11), an analogous rule can be derived for third-order tensor fields. Here, the index is $\frac{1}{3}\mathrm{sign}(ad-bc)$ with

$$a = \frac{\partial(3t_{122}-t_{111})}{\partial x}, \quad c = \frac{\partial(t_{222}-3t_{112})}{\partial x}, \tag{22}$$

and b and d are corresponding partial derivatives with respect to y. Finally, the index of a degenerate point in a fourth-order tensor field is $\frac{1}{4}\mathrm{sign}(ad-bc)$, with:

$$a = \frac{\partial(6t_{1122}-t_{1111}-t_{2222})}{\partial x} \quad c = 4\frac{\partial(t_{1222}-t_{1112})}{\partial x}. \tag{23}$$

We will draw degenerate points in red when they have a positive index, yellow when their index is negative. A more

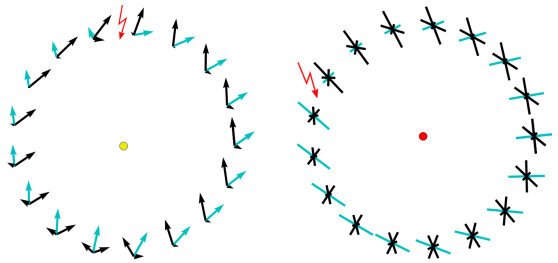

(a) Third-order tensor field (b) Fourth-order tensor field

Figure 2: *Around degenerate points (yellow/red), it is impossible to partition the vectors from the decomposition into continuous vector fields.*

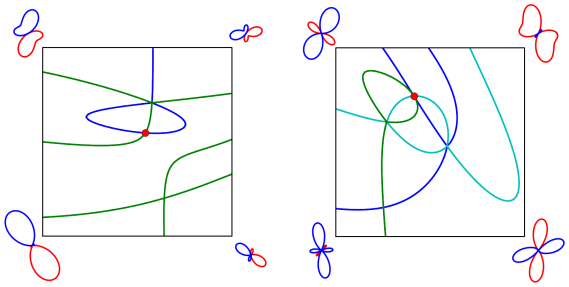

(a) Third-order tensor field (b) Fourth-order tensor field

Figure 3: *Major (blue), medium (cyan), and minor (green) lines of discontinuity on bilinear cells; tensors at the corners are shown with glyphs, degenerate points with red dots.*

detailed characterization of degenerate points, comparable to the differentiation between single and double wedges in second-order tensor topology, is left to future work.

3.5.3. Lines of Discontinuity

We have learned in the previous section that partitioning the vectors around a degeneracy inevitably leads to discontinuities. A natural way of defining vector fields that are at least piecewise continuous is to sort the rank-1 terms according to their λ_i. In this case, discontinuities in vector direction occur when $\lambda_i = \lambda_j$ for some pair $i \neq j$.

In the second-order case, this leads to the major and minor eigenvector fields, $\bar{\mathbf{v}}_1(\mathbf{x})$ and $\bar{\mathbf{v}}_2(\mathbf{x})$. Discontinuities are restricted to degenerate points, which are the only locations at which $\lambda_1 = \lambda_2$. The reason why this single equality acts as a codimension-two constraint is that it also eliminates the degree of freedom that is otherwise present in jointly rotating $\bar{\mathbf{v}}_1$ and $\bar{\mathbf{v}}_2$. In higher-order fields, the constraint $\lambda_i = \lambda_j$ only defines a codimension-one subspace, so the locations at which the constraint is fulfilled form structurally stable lines.

Rotating θ in Eq. (3) by π/ℓ amounts to multiplying one of the $\mathbf{v}_i$ by -1. For odd ℓ, the scaled $\bar{\mathbf{v}}_i$ has a fixed orientation, so the rotation flips the sign of the corresponding λ_i. To account for this indeterminacy, we sort the λ_i by absolute value in tensor fields of odd order. When talking about "larger" and "smaller" λ_i, we refer to an ordering by signed value when ℓ is even, by absolute value when ℓ is odd.

In third-order tensor fields, we can distinguish major and minor lines of discontinuity, depending on whether the larger or the smaller $|\lambda_i|$ coincide. All degenerate third-order tensors are rotated and scaled variants of the example in Fig. 1 (a). As illustrated there, $|\lambda_1| = |\lambda_2|$ and $|\lambda_2| = |\lambda_3|$ are both attained exactly once within $\theta \in [0, \pi/3)$. Since θ is rotated by $\pm 2\pi/3$ around a degeneracy, we conclude that a major and a minor line of discontinuity originate from the degeneracy, and continue through it.

In regions without a degeneracy, we can define continuous and signed, but unsorted scalar fields $\tilde{\lambda}_i(\mathbf{x})$ via a continuously varying frame of $\mathbf{v}_i$. This is analogous to locally orienting the eigenvectors in a second-order tensor field. It clarifies that lines of discontinuity are closed curves, the zero level sets of $\tilde{\lambda}_i - \tilde{\lambda}_j$ and $\tilde{\lambda}_i + \tilde{\lambda}_j$. They originate from degenerate points, but can also occur in their absence. This also helps us to understand the two cases in which lines of discontinuity in third-order tensor fields cross in absence of a degeneracy. The first occurs when $\tilde{\lambda}_i = \tilde{\lambda}_j = 0$; two lines pass through this point, corresponding to $\tilde{\lambda}_i = \tilde{\lambda}_j$ and $\tilde{\lambda}_i = -\tilde{\lambda}_j$. Since we are sorting by magnitude, they are both minor lines. The second case is $|\tilde{\lambda}_1| = |\tilde{\lambda}_2| = |\tilde{\lambda}_3|$, where the three lines $|\tilde{\lambda}_1| = |\tilde{\lambda}_2|$, $|\tilde{\lambda}_1| = |\tilde{\lambda}_3|$, and $|\tilde{\lambda}_2| = |\tilde{\lambda}_3|$ meet. This is the only location at which the type of the involved lines changes between major and minor.

In addition to rotation and scaling, degenerate fourth-order tensors can differ from the example in Fig. 1 (b) by some multiple of the identity $\alpha \mathcal{I}^{(4)}$. However, addition of an isotropic tensor only offsets all λ_i by some constant amount, so it does not influence equalities of the type $\lambda_i = \lambda_j$. We conclude from Fig. 1 (b) that all three types of lines (major, minor, and medium, which do not exist in the third-order case) will pass through a degeneracy. Moreover, $\lambda_1 = \lambda_2$ and $\lambda_3 = \lambda_4$ are attained at the same θ, so the major and minor lines will be tangential to each other.

Outside of degeneracies, major and minor lines cross without affecting each other, at any angle. Analogous to third-order tensor fields, we obtain triple crossings between major and medium ($\lambda_1 = \lambda_2 = \lambda_3$) or minor and medium ($\lambda_2 = \lambda_3 = \lambda_4$) lines, at which they change their type. Except at degenerate points, crossings of all three types of lines are non-generic. Also, minor lines no longer self-intersect, since we are now sorting by signed rather than absolute value.

Figure 3 shows lines of discontinuity in bilinear cells whose vertices have been set to randomly generated third- and fourth-order tensors, shown with polar plots. All crossings can be observed as explained in our analysis.

Lines of discontinuity are not separatrices, and a full topo-

logical analysis would additionally extract those. However, we believe that it is fundamental to fully understand the limit sets of a vector field before considering separatrices, so we concentrate on that aspect in this initial work.

4. Implementation

4.1. Extracting Degenerate Points

Just like in the vector and second order tensor case, degenerate points in third- and fourth-order tensor fields are given by two linear constraints on their coefficients, so they can be located numerically in full analogy to the methods from 2D vector and tensor topology. For details, we refer to [Tri02].

On a linear cell, substituting the parameter-dependent tensor coefficients into Eq. (12) or Eq. (16) leads to a system of two linear equations in two unknowns, which has at most one isolated solution within the cell. On a bilinear cell, it leads to a system that is quadratic in one of the variables and yields up to two isolated solutions.

4.2. Extracting Lines of Discontinuity

Unlike separatrices, which have to be integrated from certain limit points, lines of discontinuity can be identified from local information alone, based on the fact that $\lambda_i = \lambda_j$ for some $i \neq j$. Given fixed tensor coefficients, Section 3.3 provides an analytical solution for λ_i. Unfortunately, with parameter-dependent coefficients, the equations become too complex to directly solve for the curves along which $\lambda_i = \lambda_j$.

Finding lines of discontinuity numerically is facilitated by the fact that along a linearly interpolated edge, p and q in Eq. (19) change linearly, so θ varies monotonically, and by less than π/ℓ. This allows us to find the correspondence between the vector frames at the two endpoints of an edge.

The correct correspondence is determined by the rotation of the joint frame along the edge. Similar to Eq. (22) and Eq. (23), the direction of this rotation is given by the derivatives of p and q. Along a linear edge, they are proportional to $\mathbf{p}_{\text{diff}} = (p_e - p_s, q_e - q_s)^{\mathrm{T}}$, where p_s, q_s, p_e, and q_e are the values of p and q at the start and end of the edge, respectively. Define the vector $\mathbf{p}_s^{\perp} = (q_s, -p_s)^{\mathrm{T}}$. If $\mathbf{p}_s^{\perp} \cdot \mathbf{p}_{\text{diff}} > 0$, the correspondence of a vector $\mathbf{v}_i^{(s)}$ at the start of an edge is given by the unique vector $\mathbf{v}_j^{(e)}$ at its end that forms the smallest angle with $\mathbf{v}_i^{(s)}$ in counterclockwise direction. If $\mathbf{p}_s^{\perp} \cdot \mathbf{p}_{\text{diff}} < 0$, it is the closest vector in clockwise direction.

Given this correspondence, intersections between a linear edge and the feature lines can be found with an adaptive refinement scheme that is similar in spirit to a previous approach from the tensor topology literature [TKW08], but independent in its specific algorithmic steps:

1. If for any $i \neq j$, the sign of $\lambda_i - \lambda_j$ differs at the two endpoints, the edge is intersected by a line of discontinuity. Otherwise, it is ignored.
2. Approximate $\Delta = \lambda_i - \lambda_j$ by a linear function $\tilde{\Delta}(\alpha) = (1-\alpha)\Delta^{(\mathrm{s})} + \alpha\Delta^{(\mathrm{e})}$ along the edge, and solve for the position α where $\tilde{\Delta}(\alpha) = 0$. Interpolate the tensor coefficients at this point, solve for the exact values of $\lambda_i(\alpha)$ and $\lambda_j(\alpha)$, and compute the relative error
$$\delta = \frac{|\lambda_i - \lambda_j|}{|\lambda_i| + |\lambda_j|}. \tag{24}$$
3. If the second step produced a sufficiently accurate approximation ($\delta < 10^{-4}$ in our experiments), return α. Otherwise, subdivide the edge at its midpoint, and recursively apply steps 1–3 to both parts.

If we are looking for $|\lambda_i| = |\lambda_j|$, we need to consider zero crossings of $\lambda_i + \lambda_j$ in addition to those of $\lambda_i - \lambda_j$. This relatively simple method does not produce false positives and it finds the discontinuities up to the desired accuracy, but it may not find all intersections, since Δ might change sign multiple times along the edge. A higher detection rate is achieved by prescribing a minimum recursion depth. However, zero crossings can be arbitrarily close to each other, so finding them all is an ill-conditioned problem.

Computing the tangent of a line of discontinuity involves the gradients $\nabla\lambda_i$. Unfortunately, the derivatives that are easily computed from the tensor field are the gradients of the tensor components ∇t_{ijk}, and analytically deriving the Jacobian $\mathbf{J}_{t\to\lambda}$ that is needed to compute $\nabla\lambda_i$ from ∇t_{ijk} is unwieldy. Instead, from Eq. (7) and the derivatives of t_{ijk} with respect to θ, which are obtained from equations like the ones in Eq. (10), we compute the much simpler

$$\begin{aligned}\mathbf{J}^{(3)}_{\lambda\to t} &= \begin{pmatrix} \frac{\partial t_{111}}{\partial\lambda_1} & \frac{\partial t_{111}}{\partial\lambda_2} & \frac{\partial t_{111}}{\partial\lambda_3} & \frac{\partial t_{111}}{\partial\theta} \\ \vdots & \vdots & \vdots & \vdots \\ \frac{\partial t_{222}}{\partial\lambda_1} & \frac{\partial t_{222}}{\partial\lambda_2} & \frac{\partial t_{222}}{\partial\lambda_3} & \frac{\partial t_{222}}{\partial\theta} \end{pmatrix} \\ &= \begin{pmatrix} 1 & \frac{1}{8} & -\frac{1}{8} & -\frac{3}{4}\sqrt{\frac{3}{4}}(\lambda_2+\lambda_3) \\ 0 & \sqrt{\frac{3}{64}} & \sqrt{\frac{3}{64}} & \lambda_1 + \frac{5}{8}(\lambda_3-\lambda_2) \\ 0 & \frac{3}{8} & -\frac{3}{8} & -\frac{1}{4}\sqrt{\frac{3}{4}}(\lambda_2+\lambda_3) \\ 0 & \sqrt{\frac{27}{64}} & \sqrt{\frac{27}{64}} & \frac{9}{8}(\lambda_2-\lambda_3) \end{pmatrix} \end{aligned} \tag{25}$$

and obtain the derivative vector $\mathbf{d}' = (\lambda_1', \lambda_2', \lambda_3', \theta')^{\mathrm{T}}$ by solving the linear system $\mathbf{J}_{\lambda\to t}\mathbf{d}' = \mathbf{t}'$ with $\mathbf{t}' = (t'_{111}, \ldots, t'_{222})^{\mathrm{T}}$. The fourth-order version of $\mathbf{J}_{\lambda\to t}$ is

$$\mathbf{J}^{(4)}_{\lambda\to t} = \begin{pmatrix} 1 & \frac{1}{4} & 0 & \frac{1}{4} & \lambda_4 - \lambda_2 \\ 0 & \frac{1}{4} & 0 & -\frac{1}{4} & \lambda_1 - \frac{1}{2}(\lambda_2+\lambda_4) \\ 0 & \frac{1}{4} & 0 & \frac{1}{4} & 0 \\ 0 & \frac{1}{4} & 0 & -\frac{1}{4} & \frac{1}{2}(\lambda_2+\lambda_4) - \lambda_3 \\ 0 & \frac{1}{4} & 1 & \frac{1}{4} & \lambda_2 - \lambda_4 \end{pmatrix}. \tag{26}$$

Note that at degenerate points, derivatives of λ_i and θ are undefined, as $\mathbf{J}_{\lambda\to t}$ becomes singular. At any other point (x,y) on the line along which $\lambda_i - \lambda_j = 0$, we compute the 2D gradient $\mathbf{g}(x,y) = \nabla\lambda_i - \nabla\lambda_j$ by taking partial derivatives $\partial\mathbf{t}/\partial x$ and $\partial\mathbf{t}/\partial y$ in the tensor field and solving for

the partial derivatives $\partial \mathbf{d}/\partial x$ and $\partial \mathbf{d}/\partial y$ using the Jacobian $\mathbf{J}_{\lambda \to t}$, as described above. The tangent is orthogonal to $\mathbf{g}$.

These basic ideas were used to create Fig. 3. A sampling of the curves was obtained by sweeping axis-aligned edges over a bilinear grid, and each detected feature intersection is visualized with a short line segment that is aligned with the curve tangent. If some application should require an explicit representation of curve topology, our analysis provides all ingredients for tracking them: Intersection with edges can be used to find seed points, tangents and normals can be used for prediction and correction steps, and the analysis in Section 3.5.3 clarifies which bifurcations must be treated.

5. Experiments

5.1. Higher-Order Derivatives

Just like the first-order partial derivatives of a smooth scalar field $f(\mathbf{x})$ make up the gradient vector $\nabla f(\mathbf{x})$, and the second-order derivatives form the symmetric Hessian matrix $\mathbf{H}(\mathbf{x})$, third-order partial derivatives $\partial^3 f(\mathbf{x})/\partial x_i \partial x_j \partial x_k$ produce a symmetric third-order tensor field $\mathcal{T}(\mathbf{x})$.

We have computed such third-order derivatives from three synthetic MR images, created using the BrainWeb [CKK*97] normal brain template with T_1 weighting and 1 mm slice thickness. The first example (closeup in Fig. 4 (a)) is noise-free. In the second and third case, we added 3% (Fig. 4 (b)) and 5% (Fig. 4 (c)) noise with respect to white matter signal intensity and a spatially varying gain field, which multiplies image intensities by values in the range of $[0.8, 1.2]$. Such bias arises from different sources [STBA94] and varies over the image in complex shapes. The noisy images were also rotated by 10° to simulate subject motion between acquisitions.

The third-order tensors were interpolated bilinearly, and degenerate points were extracted. Even though they do not have a clear interpretation in terms of the depicted brain anatomy, the same is true for image keypoints that are presently used in computer vision [TM08]. Such features can provide useful landmarks for tasks like image registration, tracking, or object recognition if we are able to reliably recover and match them in a transformed version of the image, no matter if they have a clear semantic interpretation.

In Fig. 4 (b) and (c), the degeneracies from the perturbed images are rendered as crosses. To facilitate the comparison, the features from (a) are rotated with the image and overlaid as circles. Few features vanish in the degraded image, even though some are introduced by the noise. A large number of the feature points remain close to their original locations, and preserve their type (index). The degenerate points benefit from their invariance under rotation and uniform scaling, which reduces the impact of the gain field. The fact that higher-order derivatives are sensitive to noise can be addressed by scale space analysis [Lin98]. Our experiment

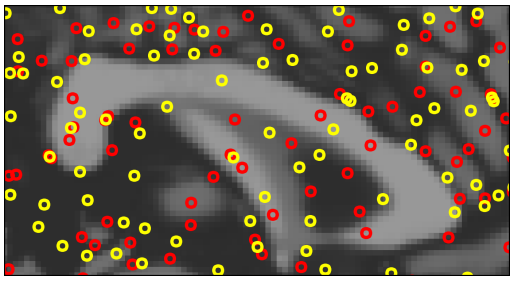

(a) Third-order degeneracies in a noise-free synthetic MR image.

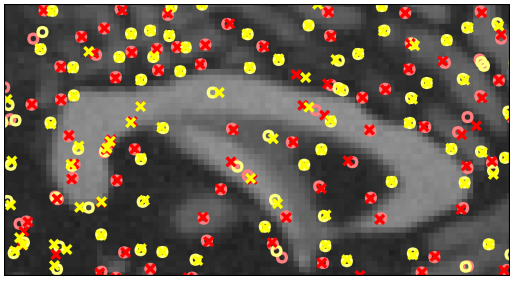

(b) Rotation, noise, and spatially varying gain applied to (a).

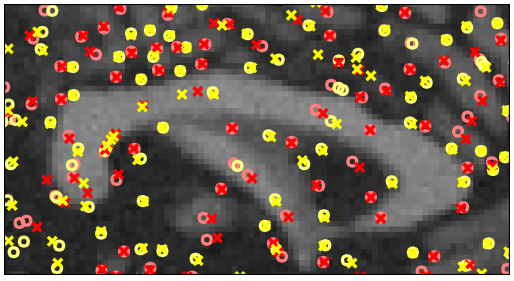

(c) Same as (b), with higher level of noise.

Figure 4: *Degeneracies in third-order derivatives provide feature points that are fairly robust under rotation and typical MR image degradations. For comparison, points from (a) are overlaid on (b) and (c) as circles.*

used a fixed Gaussian scale $\sigma = 2$; we plan to study the persistence of our features over scale as part of our future work, and we hope to evaluate their merit relative to more established keypoints from the computer vision literature.

5.2. Higher-Order Structure Tensors

Given a color image as a vector-valued function $\mathbf{f}(\mathbf{x})$ over some image domain $\Omega \subset \mathbb{R}^2$, its order-$\ell$ structure tensor $\mathcal{S}_\rho(\mathbf{x})$ at scale ρ is defined as [SWS09]

$$\mathcal{S}_\rho(\mathbf{x}) = G_\rho \star \sum_{i=1}^{3} \left(\frac{\nabla f_i(\mathbf{x})}{\|\nabla f_i(\mathbf{x})\|^{\frac{\ell-2}{\ell}}} \right)^{\otimes \ell} . \qquad (27)$$

Here, $G_\rho \star$ denotes convolution with a Gaussian kernel with standard deviation ρ, and the sum is taken over RGB components $f_i(\mathbf{x})$.

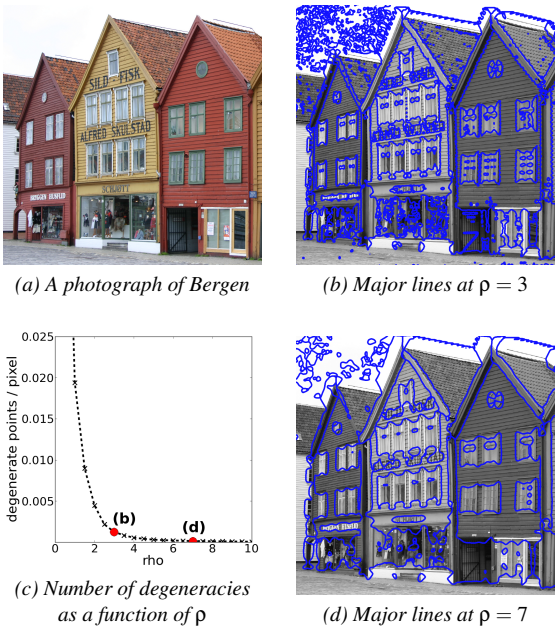

(a) A photograph of Bergen *(b) Major lines at* $\rho = 3$

(c) Number of degeneracies as a function of ρ *(d) Major lines at* $\rho = 7$

Figure 5: *The major lines of discontinuity in the higher-order structure tensor field of a given image (a) indicate meaningful regions at different scales (b/d).*

The major eigenvector of a second-order structure tensor provides an estimate of the locally dominant gradient direction [Di 86]. We have found experimentally that the major vector field $\bar{\mathbf{v}}_1(\mathbf{x})$ from the constrained decomposition of a fourth-order structure tensor is generally closely aligned with this estimate, except around the lines of discontinuity. The analysis in Section 3.5.3 has shown that these lines are closed, so they partition the image domain Ω into regions in which the fourth-order structure tensor estimate of the principal gradient direction varies continuously.

Figure 5 illustrates these lines in a structure tensor field that has been computed from a color image of Bergen, Norway. The black-and-white version is only used for visualization, to distract less from the lines. The major lines of discontinuity are clearly related to semantic structures in the picture, like the windows and rooftops of the houses, even though they are less expressive when no clear gradients are present (e.g., in the sky region).

The level of detail in the lines varies with the chosen scale ρ. Using the number of degenerate points as a measure of topological complexity, Figure 5 (c) shows that many unstable features exist at small scales ($\rho < 2$). Major features, such as the ones in Subfigure (d), are preserved up to much larger scales. In the future, it would be interesting to track these features over scale, to study the topology at even higher orders ($\ell = 6$ or $\ell = 8$), and to combine it with the idea of nonlinear structure tensors [BWBM06]. Possibly, this approach could be refined sufficiently to serve as an ingredient in a method for unsupervised texture segmentation.

6. Conclusion and Future Work

Methods for the extraction of geometric features from higher-order tensor fields are needed to achieve concise and effective visualizations, but are largely unexplored. Similar to previous work on second-order tensor fields [DH94, ZPP05], we have approached this problem from a mathematical, application-independent perspective, by formally extending established concepts of topological visualization to 2D symmetric higher-order tensor fields, and studying the resulting structures.

Starting from the observation that a continuous decomposition into a unique set of vectors is required to apply the concepts of vector field topology, we derived an analytical solution for a geometrically constrained decomposition [KE10]. We showed that, at least for orders $\ell = 3$ and $\ell = 4$, it leads to continuous and unique results, except at isolated degenerate points, which provide topological features.

This allowed us to derive vector fields that contain all the information from the higher-order tensor field. Due to the fractional Poincaré index of the degenerate points, these vector fields are only piecewise continuous. The lines along which discontinuities occur are a new type of topological feature. We clarified their behavior for orders three and four. We have developed algorithms to numerically extract degenerate points and lines of discontinuity, and applied them to higher-order derivatives and higher-order structure tensors.

The geometric constraint from [KE10] is the only symmetric higher-order tensor decomposition that we are presently aware of that yields unique vector fields, and thus lends itself to topological analysis. Our future work will try to identify alternative constraints that may lead to unique and efficiently computable tensor decompositions, and might be more interpretable in applications such as diffusion imaging. Since many medical and scientific datasets are three-dimensional, we will also pursue 3D tensor decompositions.

We believe that ultimately, the combination of application-specific constraints and reliable numerical methods for tensor decomposition will allow us to produce expressive visualizations of higher-order tensor fields, a type of scientific data whose complexity still presents a challenge at the current state of the art. We consider our present work an important first step towards that goal.

Acknowledgements

I would like to thank Lek-Heng Lim and Gordon Kindlmann (University of Chicago) for valuable discussions. This work was supported by a fellowship within the Postdoc Program of the German Academic Exchange Service (DAAD).

References

[BPS98] BAJAJ C., PASCUCCI V., SCHIKORE D.: Visualization of scalar topology for structural enhancement. In *Proc. IEEE Visualization* (1998), Ebert D. S., Rushmeier H., Hagen H., (Eds.), pp. 51–58.

[BWBM06] BROX T., WEICKERT J., BURGETH B., MRÁZEK P.: Nonlinear structure tensors. *Image and Vision Computing 24*, 1 (2006), 41–55.

[CGLM08] COMON P., GOLUB G., LIM L.-H., MOURRAIN B.: Symmetric tensors and symmetric tensor rank. *SIAM Journal on Matrix Analysis and Applications 30*, 3 (2008), 1254–1279.

[CKK*97] COCOSCO C. A., KOLLOKIAN V., KWAN R. K.-S., PIKE G. B., EVANS A. C.: BrainWeb: Online interface to a 3D MRI simulated brain database. *NeuroImage (Proc. Int'l Conf. Functional Mapping of the Human Brain) 5*, 4 (1997), S425. http://www.bic.mni.mcgill.ca/brainweb/.

[CM96] COMON P., MOURRAIN B.: Decomposition of quantics in sums of powers of linear forms. *Signal Processing 53*, 2 (1996), 96–107.

[Dam98] DAMON J.: Generic structure of two-dimensional images under gaussian blurring. *SIAM Journal on Applied Mathematics 59*, 1 (1998), 97–138.

[DH93] DELMARCELLE T., HESSELINK L.: Visualizing second-order tensor fields with hyperstreamlines. *IEEE Computer Graphics and Applications 13*, 4 (1993), 25–33.

[DH94] DELMARCELLE T., HESSELINK L.: The topology of symmetric, second-order tensor fields. In *Proc. IEEE Visualization* (1994), Bergeron R. D., Kaufman A. E., (Eds.), pp. 140–147.

[Di 86] DI ZENZO S.: A note on the gradient of a multi-image. *Computer Vision, Graphics, and Image Processing 33* (1986), 116–125.

[HH89] HELMAN J., HESSELINK L.: Representation and display of vector field topology in fluid flow data sets. *Computer 22*, 8 (1989), 27–36.

[HS05] HLAWITSCHKA M., SCHEUERMANN G.: HOT-lines: Tracking lines in higher order tensor fields. In *Proc. IEEE Visualization* (2005), Silva C., Gröller E., Rushmeier H., (Eds.), pp. 27–34.

[Jac46] JACOBI C. G. J.: Über ein leichtes verfahren die in der theorie der säcularstörungen vorkommenden gleichungen numerisch aufzulösen. *Journal für die reine und angewandte Mathematik 30* (1846), 51–94.

[KB09] KOLDA T. G., BADER B. W.: Tensor decompositions and applications. *SIAM Review 51*, 3 (2009), 455–500.

[KE10] KYRGYZOV O. O., ERDOGMUS D.: Numerical optimization of a sum-of-rank-1 decomposition for n-dimensional order-p symmetric tensors. *Neurocomputing 73*, 16–18 (2010), 3323–3327.

[Kyr10] KYRGYZOV O. O.: *Non-redundant Tensor Decomposition*. PhD thesis, Northeastern University, Boston MA, 2010.

[Lin98] LINDEBERG T.: Edge detection and ridge detection with automatic scale selection. *International Journal of Computer Vision 30*, 2 (1998), 117–154.

[NBJ*08] NEEMAN A. G., BRANNON R., JEREMIĆ B., VAN GELDER A., PANG A.: Decomposition and visualization of fourth-order elastic-plastic tensors. In *IEEE/EG Symposium on Volume and Point-Based Graphics* (2008), Hege H.-C., Laidlaw D., Pajarola R., Staadt O., (Eds.), pp. 121–128.

[ÖM03] ÖZARSLAN E., MARECI T.: Generalized diffusion tensor imaging and analytical relationships between diffusion tensor imaging and high angular resolution diffusion imaging. *Magnetic Resonance in Medicine 50* (2003), 955–965.

[PVH*03] POST F. H., VROLIJK B., HAUSER H., LARAMEE R. S., DOLEISCH H.: The state of the art in flow visualisation: Feature extraction and tracking. *Computer Graphics Forum 22*, 4 (2003), 775–792.

[PZ07] PALACIOS J., ZHANG E.: Rotational symmetry field design on surfaces. *ACM Transactions on Graphics (Proc. ACM SIGGRAPH) 26*, 3 (2007), 55.

[Rez92] REZNICK B. A.: Sums of even powers of linear forms. *Memoirs of the American Mathematical Society 96*, 463 (1992), 1–155.

[SK10] SCHULTZ T., KINDLMANN G.: A maximum enhancing higher-order tensor glyph. *Computer Graphics Forum (Proc. EuroVis) 29*, 3 (2010), 1143–1152.

[SNAHH11] SREEVALSAN-NAIR J., AUER C., HAMANN B., HOTZ I.: Eigenvector-based interpolation and segmentation of 2D tensor fields. In *Topological Methods in Data Analysis and Visualization*, Pascucci V., Tricoche X., Hagen H., Tierny J., (Eds.). Springer, 2011, pp. 139–150.

[SS08] SCHULTZ T., SEIDEL H.-P.: Estimating crossing fibers: A tensor decomposition approach. *IEEE Transactions on Visualization and Computer Graphics (Proc. IEEE Visualization) 14*, 6 (2008), 1635–1642.

[STBA94] SIMMONS A., TOFTS P. S., BARKER G. J., ARRIDGE S. R.: Sources of intensity nonuniformity in spin echo images at 1.5 T. *Magnetic Resonance in Medicine 32*, 1 (1994), 121–128.

[STS07] SCHULTZ T., THEISEL H., SEIDEL H.-P.: Topological visualization of brain diffusion MRI data. *IEEE Transactions on Visualization and Computer Graphics (Proc. IEEE Visualization) 13*, 6 (2007), 1496–1503.

[SWS09] SCHULTZ T., WEICKERT J., SEIDEL H.-P.: A higher-order structure tensor. In *Visualization and Processing of Tensor Fields – Advances and Perspectives*, Laidlaw D. H., Weickert J., (Eds.). Springer, 2009, pp. 263–280.

[TKW08] TRICOCHE X., KINDLMANN G., WESTIN C.-F.: Invariant crease lines for topological and structural analysis of tensor fields. *IEEE Transactions on Visualization and Computer Graphics (Proc. IEEE Visualization) 14*, 6 (2008), 1627–1634.

[TM08] TUYTELAARS T., MIKOLAJCZYK K.: Local invariant feature detectors: A survey. *Foundations and Trends in Computer Graphics and Vision 3*, 3 (2008), 177–280.

[Tri02] TRICOCHE X.: *Vector and Tensor Field Topology Simplification, Tracking, and Visualization*. PhD thesis, Fachbereich Informatik, Universität Kaiserslautern, 2002.

[TSH01] TRICOCHE X., SCHEUERMANN G., HAGEN H.: Tensor topology tracking: A visulization method for time-dependent 2D symmetric tensor fields. *Computer Graphics Forum 20*, 3 (2001), 461–470.

[ZP05] ZHENG X., PANG A.: 2D asymmetric tensor analysis. In *Proc. IEEE Visualization* (2005), Silva C., Gröller E., Rushmeier H., (Eds.), pp. 3–10.

[ZPP05] ZHENG X., PARLETT B., PANG A.: Topological lines in 3D tensor fields and discriminant hessian factorization. *IEEE Transactions on Visualization and Computer Graphics 11*, 4 (2005), 395–407.

[ZYLL09] ZHANG E., YEH H., LIN Z., LARAMEE R. S.: Asymmetric tensor analysis for flow visualization. *IEEE Transactions on Visualization and Computer Graphics 15*, 1 (2009), 106–122.